Indian Journal of Pure & Applied Physics
Vol. 63, January 2025, pp. 22-33
DOI: 10.56042/ijpap.v63i1.9803

Crystal Structure Analysis using Rietveld Refinement and Investigation of Electrical Properties of $NaNbO_3$ Substituted $CaTiO_3$ Ceramics

M Sindhu[a], N Ahlawat[b], S Sanghi[b], R Kumari[b], D Nandal[c], V Nandal[d], L Kumar[e*], N Mittal[e], V S Pandey[f] & A Agarwal[b]

[a]Department of Physics, Govt. College Dujana, Jhajjar 124 102, Haryana, India

[b]Department of Physics, Guru Jambheshwar University of Science and Technology, Hisar 125 001, Haryana, India

[c]Department of Computer Science & Engineering, Guru Jambheshwar University of Science and Technology, Hisar 125 001, Haryana, India

[d]Department of Electronics, UIET, MDU, Rohtak 124 001, Haryana, India

[e]Department of Industry 4.O, Shri Vishwakarma Skill University, Palwal 121 102, Haryana, India

[f]Department of Physics, National Institute of Technology, Delhi 110 036, India

Received 22 March 2024; accepted 17 December 2024

Polycrystalline samples (1-x)$CaTiO_3$-x$NaNbO_3$ (x = 0, 0.10, 0.20, 0.30 and 0.40) were synthesized using solid state reaction method. Powder X-ray diffraction at room temperature showed that all of the samples' crystal structures were orthorhombic with Pbnm space group. Low χ^2 values were obtained and there was good agreement between the computed and observed XRD patterns according to the Rietveld refinement. Impedance spectroscopy of the samples was investigated over a broad frequency and temperature range. Nyquist plots of the samples depicted a thermally activated non-Debye type relaxation mechanism. A decrease in dispersive nature of dielectric constant (ε′) and tangent loss (tan δ) at low frequencies is noticed in the $NaNbO_3$ substituted samples rendering them a better stability. The samples became more resistive with $NaNbO_3$ substitution in $CaTiO_3$ lattice. Correlation between charge carriers and lattice has been established using modulus formalism. Imaginary impedance (Z′′) and imaginary modulus (M′′) have been employed to comprehend the conduction process in all the samples.

Keywords: Rietveld refinement; Titanates; Impedance spectroscopy

1 Introduction

Ceramic-based dielectric capacitors have garnered significant attention for high-power electronic systems because of high power density and good thermal stability[1-3]. Below 30K, $CaTiO_3$ exhibits a saturation of the dielectric permittivity, behaving as a quantum paraelectric or an incipient ferroelectric[4]. This material can therefore serve as a worthy contender for the future generation of communication devices[5]. $CaTiO_3$ based ceramic solid solutions are one of the high-quality microwave dielectric materials[6]. At various temperatures, $CaTiO_3$ exhibits four distinct space groups: tetragonal (I4/mcm), orthorhombic (Pbnm), orthorhombic (Cmcm), and cubic (Pmm). It exists in the orthorhombic phase (Pbnm)[7] at room temperature. At high temperatures (above 1580 K) it has an ideal perovskite structure and shows cubic phase[8]. At room temperature, $NaNbO_3$ is an antiferroelectric; but, at low temperatures, it turns ferroelectric. Among the oxygen octahedral perovskites, $NaNbO_3$ exhibits the most structural phase changes between the nonferroelectric (NF), antiferroelectric (AFE), and ferroelectric (FE) phases[9]. In general, six phase transitions are present within the range of T = 923 K to T = 153 K[10]. The reversible AFE-to-FE phase transition, induced by the electric field, gives AFE ceramics unique double polarization-electric field hysteresis loops and a large polarization difference. This leads to remarkable improvements in energy storage density compared to the linear dielectric and relaxor FE ceramics[1,11-13]. The large polarization hysteresis in the AFE-FE phase transition typically leads to low energy-storage efficiency in normal AFE ceramics. However, incorporating dielectric relaxation characteristics into these materials has lately proven effective in augmenting their energy-storage performance[14-17]. NaNbO3 (NN)-based lead-free AFE ceramics possess robust prospective for energy-storage applications due to their wide band gaps and low cost. These

*Corresponding author: (E-mail: lalitkumar_khanna@yahoo.com)

advantages make them competitive compared to other lead-free AFE materials[15,18-20].

In environmentally friendly lead-free materials, the solid solutions that are studied consist of one or both the components to be ferroelectrics at room temperature. At room temperature, however, neither of the end members in the $CaTiO_3$-$NaNbO_3$ solid solution are ferroelectric or piezoelectric. As studied by Tripathi *et al*. the solid solutions of $xCaTiO_3$-(1-x) $NaNbO_3$ show behavior similar to the morphotropic phase boundary (MPB) in an intermediate composition range ($0.10 < x < 0.20$) in a non-ferroelectric system.[21]. Unlike the well-known MPB systems, which are all ferroelectric and piezoelectric in nature, these ceramics offer the first example of a non-ferroelectric and non-piezoelectric MPB system. Na^+ is substituted at the Ca^{2+} site in this system to ensure local level charge compensation[22]. Whereas the substitution of Ti^{4+} with much heavier Nb^{5+} reduces the zero-point vibrational energy and thus facilitates low-temperature phase stabilization in $CaTiO_3$ matrix[22].

In this study (1-x)$CaTiO_3$-x$NaNbO_3$ lead free ceramics have been produced by using the solid state reaction technique to concurrently substitute Na^+ at the A-site and Nb^{5+} at the B-site in $CaTiO_3$. XRD has been used for structural analysis at room temperature. All of the samples have undergone additional, in-depth structural analysis using the GSAS+EXPGUI tool and Rietveld refinement. The investigation of electrical properties has been performed via impedance spectroscopy across a broad frequency range and at various temperatures. To analyze the dynamics of charge carriers, modulus formalism is used.

2 Experimental Details

The solid state reaction technique was utilized to synthesize polycrystalline (1-x)$CaTiO_3$-x$NaNbO_3$ (x = 0.0, 0.10, 0.20, 0.30, 0.40; abbreviated as CT, CTNN1, CTNN2, CTNN3, and CTNN4 respectively) samples at high temperatures. The raw materials used were analytical reagent grade (purity 99.0%) $CaCO_3$, TiO_2, Na_2CO_3, and Nb_2O_5. To create microscopic particles, the powders were combined in an exact stoichiometric ratio and ground in an agate mortar. After that, the mixes were calcined for six hours at a ramp of 5 K/min at 873 K. Once more, the calcined powders were ground for 30 min and then sintered at 1573-1673K from 4-6h. A Rigaku Miniflex-II diffractometer with Cu Kα radiation (2θ range (10-80º) and a scanning rate of 1^0 min^{-1} with a scan step of 0.02^0 was used to study the ceramic structures using X-ray diffraction at ambient temperature. The software GSAS+EXPGUI was used to acquire the lattice parameters and structural refinement[23,24]. The grain morphology of the samples (SEM; JEOL JSM-6610/LV, USA) was investigated using scanning electron microscopy. To quantify the sample's electrical characteristics, powder with 3% PVA as binder, was uniaxially pressed (10-ton pressure) to form compact discs. Next, discs were sintered at the 1573-1673K for 4-6h. On the opposing faces of the disc, silver electrodes were deposited, and impedance testing was carried out over a wide range of frequencies and temperatures using an impedance/ gain-phase analyzer (Newton's 4th Ltd.).

3 Results and discussion

3.1 Structural studies

To ascertain the phase composition of the sintered samples, XRD analysis was performed. The room temperature XRD patterns of the sintered CT and CTNN samples are displayed in Fig. 1. CT sample is reported elsewhere[25]. All of the compositions show a pure polycrystalline perovskite structure, and the samples don't contain any impurity phases. $NaNbO_3$ appears to have diffused in the CT lattice in the CTNN samples to form a solid solution. CT at room temperature exhibits an orthorhombic phase. The room temperature XRD patterns of CTNN samples were found to have similar peak profiles as the CT sample at room temperature. Thus, suggesting CTNN samples at room temperature also exhibited

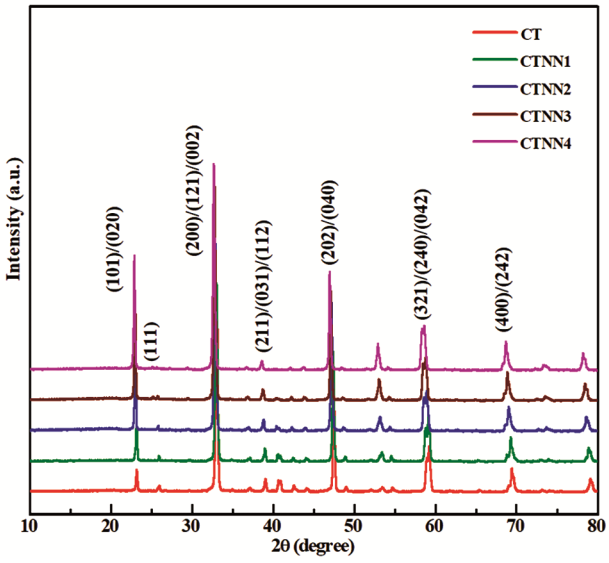

Fig. 1 — XRD patterns of CT, CTNN1, CTNN2, CTNN3 and CTNN4 samples at room temperature.

orthorhombic phase. The XRD peak profiles clearly move towards lower angles in Fig. 1, which indicates a rise in the lattice constants. The XRD patterns were structurally studied by Rietveld refinement (GSAS+EXPGUI) for additional confirmation and detailed study of the structure. The Rietveld method refines a theoretical line profile using a least -square approach until it matches the measured profile. For Rietveld refinement, a structural model that approximates the real structure is necessary. This approach treats the whole spectrum, including the intensity of the background, as a single discrete function that must be fitted with a multi-parameter model. Agreement indices or residuals (R_p, R_{wp}) are used to obtain convergence and make refinement more quantitative, thus approaching χ^2 (goodness of fit) towards unity[26]. Figs. 2(a-e) shows the simulated and experimental XRDs for each sample. A reasonably good fit exists between the estimated and experimental spectra on the basis of comparatively lower R_p and R_{wp} (<10%) values. The goodness of fit (GOF) for structure, peak forms, and background is estimated using profile R-factors. The zero-point shift for studied XRD patterns was corrected using Si (640c) powder as a standard. Before refining unit cell and the background parameters, Systemic errors like zero-point shift were taken into consideration when doing the initial Rietveld refining. It was supposed that the peak form was a pseudo-Voigt function. Chebyschev polynomial of the first kind was used to rectify the background. To improve the fit, the following parameters were changed: the scale factor, occupancy, atomic functional positions, lattice parameters, peak profile parameters, and isotropic thermal parameters. The Pbnm space group is said to exist in CT at room temperature. As a result, because of the orthorhombic perovskite structure's Pbnm space group, all CTNN samples could be refined. It is clear that the simulated and experimental relative intensities accord quite well. Table 1 lists each sample's profile R-factors and enhanced structural attributes. Table 2 provides the bond lengths, bond angles, and tolerance factor. Fig. 3(a) represents the variation of lattice parameters and Fig. 3(b) represents the variation of unit cell volume for the synthesized samples[27]. When the $NaNbO_3$ content of the $CaTiO_3$ lattice indicated in Table 1 grew, so did the lattice parameters ‘a’, ‘b’ and ‘c’. This also resulted in volume of the lattice increasing with increase in $NaNbO_3$ content. This could be explained by the fact that the ions Na and Nb have larger ionic radii than ions Ca and Ti. The octahedron's tilting angle with respect to plane 001 is represented by the bond angle Ti-O1-Ti, and its rotation around the c-axis is shown by the Ti-O_2-Ti angle. Both of these angles, which are less than 180^0 (Table 2), show how the polyhedral TiO_6 rotates. The degree to which the structure deviates from the ideal cubic is determined by the tolerance factor (t). The value assigned to ‘t’ for a perfect cubic perovskite is unity. In perovskites with ‘t’ values lesser than one the oxygen polyhedral buckles as there is lesser space available. The tolerance factor for CT and CTNN ceramics calculated from the bond lengths obtained by structure refinement are given in Table 2. All the prepared CT and CTNN samples have a tolerance factor less than unity.

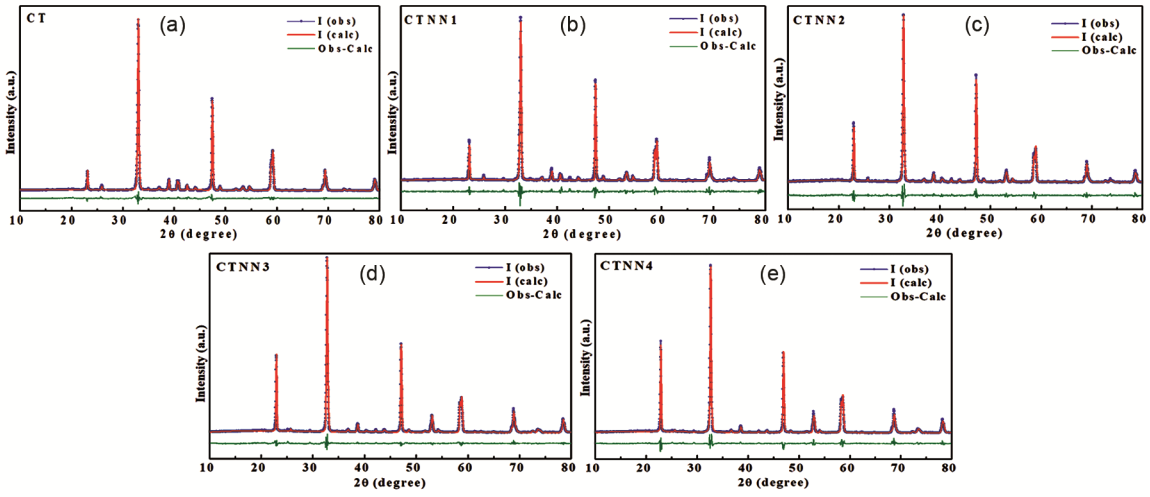

Fig. 2 — Observed, calculated and difference Rietveld refined XRD patterns of (a) CT (b) CTNN1 (c) CTNN2 (d) CTNN3 (e) CTNN4 samples.

Table 1 — Rietveld refinement parameters of CT, CTNN1, CTNN2, CTNN3 and CTNN4 sampless

Sample	Structural Phase model	Lattice Parameters	Atomic positions	R-factors (%)
CT	Orthorhombic Pbnm	a=5.387 Å b=5.435 Å c=7.644 Å V=223.814 Å^3	Ca(0.006, 0.032, 0.25) Ti(0, 0.5, 0) O1(0.572, -0.018, 0.25) O2(0.285, 0.289, 0.038)	χ^2 = 1.68 R_{wp} = 5.55 R_p = 4.16
CTNN1	Orthorhombic Pbnm	a=5.398 Å b=5.447 Å c=7.659 Å V=225.220 Å^3	Ca/Na(0.012, 0.029, 0.25) Ti/Nb(0, 0.5, 0) O1(0.592, -0.018, 0.25) O2(0.282, 0.285, 0.039)	χ^2 = 3.84 R_{wp} = 8.90 R_p = 7.54
CTNN2	Orthorhombic Pbnm	a=5.406 Å b=5.457 Å c=7.679 Å V=226.525 Å^3	Ca/Na(0.007, 0.032, 0.25) Ti/Nb(0, 0.5, 0) O1(0.557, -0.009, 0.25) O2(0.289, 0.285, 0.039)	χ^2 = 3.43 R_{wp} = 8.79 R_p = 7.32
CTNN3	Orthorhombic Pbnm	a=5.417 Å b=5.468 Å c=7.696 Å V=227.956 Å^3	Ca/Na(0.007, 0.032, 0.25) Ti/Nb(0, 0.5, 0) O1(0.568, -0.009, 0.25) O2(0.285, 0.288, 0.038)	χ^2 = 1.97 R_{wp} = 5.55 R_p = 4.64
CTNN4	Orthorhombic Pbnm	a=5.429 Å b=5.471 Å c=7.706 Å V=228.872 Å^3	Ca/Na(0.009, 0.028, 0.25) Ti/Nb(0, 0.5, 0) O1(0.566, -0.012, 0.25) O2(0.286, 0.282, 0.037)	χ^2 = 2.78 R_{wp} = 7.51 R_p = 9.55

Table 2 — Bond lengths, bond angles and tolerance factor for CT and CTNN samples obtained from Rietveld refinement

Bond Type	Bond Length (Å)	Tolerance Factor	Bond Angles (^{O})
CT			
Ca--O1 x 1	2.340, 2.478, 3.023, 3.078	0.985	Ti-O1-Ti 155.9
Ca--O2 X 2	2.375, 2.637, 2.672, 3.211		Ti-O2-Ti 155.9
Ti--O1 X 2	1.954		
Ti --O2(A) X 2	1.965		
Ti --O2(B) X 2	1.949		
CTNN1			
Ca/Na--O1 x 1	2.531, 2.280, 3.032, 3.143	0.983	Ti-O1-Ti 150.3
Ca/Na--O2 X 2	2.367, 2.734, 3.218, 3.586		Ti-O2-Ti 156.6
Ti/Nb--O1 X 2	1.981		
Ti/Nb--O2(A) X 2	1.971		
Ti/Nb--O2(B) X 2	1.945		
CTNN2			
Ca/Na--O1 x 1	2.439, 2.984, 2.974, 2.527	0.987	Ti-O1-Ti 161.4
Ca/Na--O2 X 2	2.377, 2.621, 2.702, 3.238		Ti-O2-Ti 155.6
Ti/Nb--O1 X 2	1.945		
Ti/Nb--O2(A) X 2	1.977		
Ti/Nb --O2(B) X 2	1.953		
CTNN3			
Ca/Na--O1 x 1	2.392, 2.543, 2.987, 3.044	0.986	Ti-O1-Ti 158.1
Ca/Na--O2 X 2	2.377, 2.699, 2.635, 3.251		Ti-O2-Ti 155.5
Ti/Nb--O1 X 2	1.959		
Ti/Nb --O2(A) X 2	1.972		
Ti/Nb--O2(B) X 2	1.966		
CTNN4			
Ca/Na--O1 x 1	2.419, 2.543, 2.988, 3.029	0.988	Ti-O1-Ti 158.7
Ca/Na--O2 X 2	2.397, 2.621, 2.727, 3.218		Ti-O2-Ti 157.2
Ti/Nb--O1 X 2	1.960		
Ti/Nb--O2(A) X 2	1.979		
Ti/Nb--O2(B) X 2	1.952		

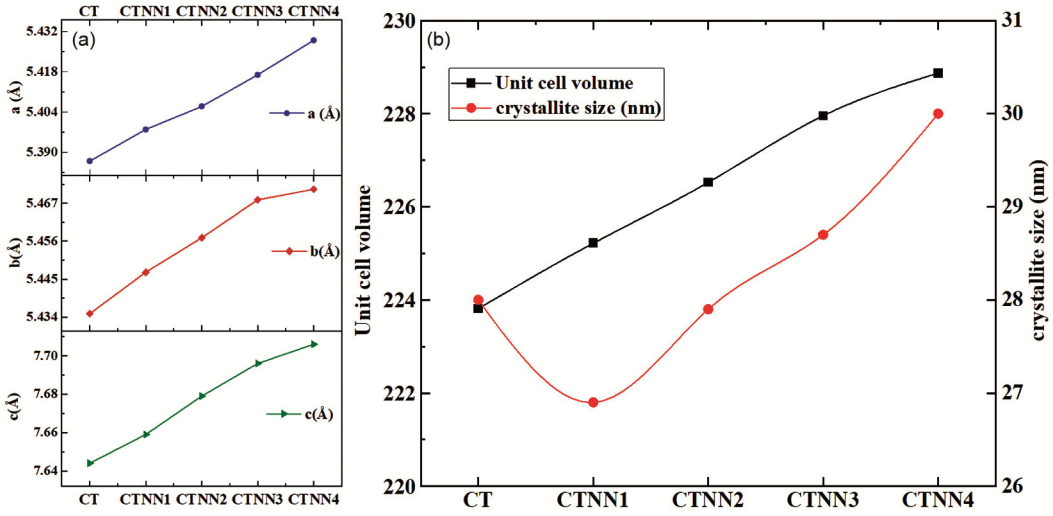

Fig. 3 — (a)Variation of lattice parameters 'a', 'b', 'c'(b) Variation of unit cell volume and crystallite size for CT, CTNN1, CTNN2, CTNN3 and CTNN4 samples.

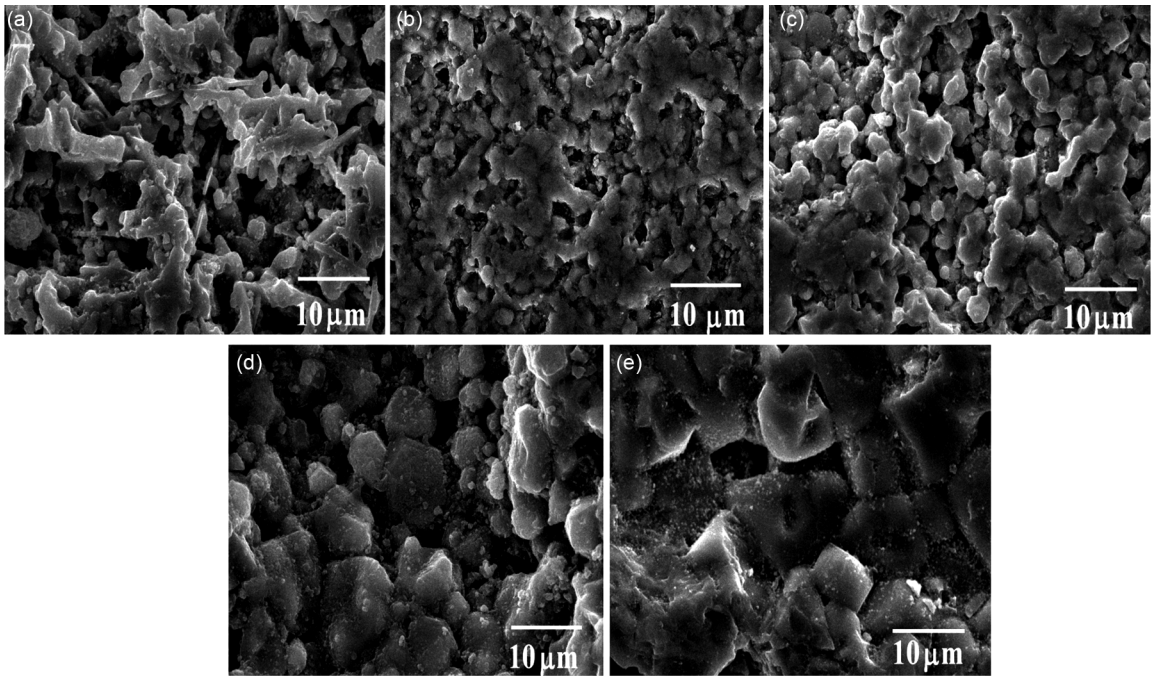

Fig.4 — SEM images of (a) CT (b) CTNN1 (c) CTNN2 (d) CTNN3 (e) CTNN4 samples.

The average crystallite size (D) was calculated for the most intense peak (121) in the XRD spectra using the Debye Scherrer relation[28-31], $D = \frac{K\lambda}{\beta cos\theta}$ where K is a constant (0.91), λ is the characteristic X-ray wavelength (1.54 Å), β is the FWHM in radians and θ is the Bragg's angle. The average crystallite size thus obtained is 28 nm, 26.9 nm, 27.9 nm, 28.7 nm and 30 nm for CT, CTNN1, CTNN2, CTNN3 and CTNN4 samples respectively (Fig. 3 (b)). The SEM analysis was done on the surface for CT and CTNN samples. The micrographs in Fig. 4 revealed a non-uniform (as shape and size) granular microstructure. The SEM images clearly depicted increased grain size with increased $NaNbO_3$ content in these ceramics. It can also be seen in the images that porosity in the samples has decreased with increased $NaNbO_3$ content. This suggests an increase in density of the samples with increase of $NaNbO_3$ concentration in the CT lattice. Uniformity in size of grains is also seen as

the $NaNbO_3$ content increased. Uniform angular grains due to higher content of $NaNbO_3$ can be seen in the CTNN4 sample.

3.2 Impedance studies

The Nyquist plots that are graphical representation of impedance (Z) in complex plane provide significant details about the electrical properties of the system being investigated. Henceforth the Nyquist diagrams for all the samples at different temepratures have been studied. Fig. 5 shows complex impedance spectra for CTNN3 sample at various temperatures. As temperature increased a decrease in the impedance was observed (Fig. 5) and the centre of arc shifted towards the origin. This suggested that the relaxation process was thermally activated. A relaxation mechanism other than the Debye type was revealed by the slightly depressed semicircular arcs.Similar behaviour was observed for all the prepared samples. Fig. 6 depicts the normalised impedance spectra of CT and CTNN samples at 673K. The intersection point of the semicircular arc on the real axis in the normalised impedance spectra gives the value of resistivity of all the samples. The resistivity thus calculated isgiven in Table 3. The resistivity values increased significantly with introduction of $NaNbO_3$ inthe CT matrix. It can be clearly observed from the plots that with increase of $NaNbO_3$ upto 30%, resistivity of the samples increased however further increase in concentration of $NaNbO_3$ did not effect the resistivity values much and it was almost similar for CTNN3 and CTNN4 samples. The observed increase in resitivity suggests low mobility of ions in the lattice which may be attributed to the heavy ions Na^+ and rietveld in comparison to the Ca^{2+} and Ti^{4+} ions.The increased density of the samples as depicted by the SEM images may also be the reason for lower mobility of ions.

3.3 Dielectric studies

The frequency dependence of the dielectric constant (ε') and dielectric loss (tan δ) for CT and

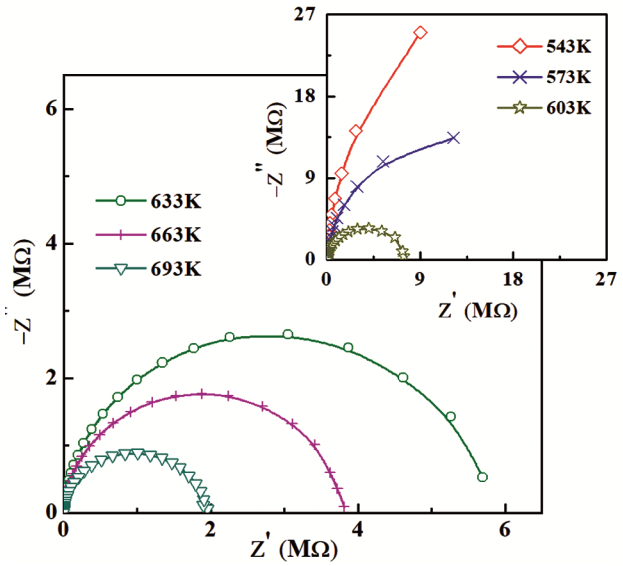

Fig. 5 — Impedance spectra of CTNN3 sample at different temperatures.

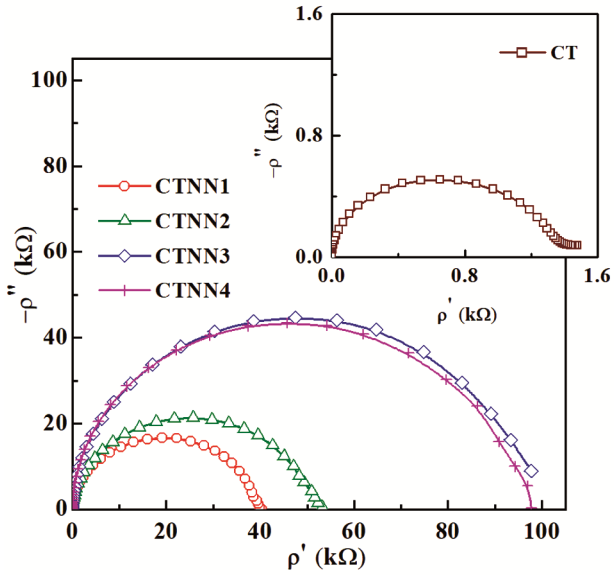

Fig. 6 — Normalised impedance spectra for CT and CTNN samples at 673K.

Table 3 — Resistivity (ρ), dc conductivity (σ_{dc}), ac conductivity (σ_{ac}), fractional components (s_1) and (s_2), dielectric constant (ε′), dielectric loss (tan δ), stretching coefficient (β) and relaxation times ($\tau_{M''}$) for CT and CTNN samples

Sample	ρ (10^5Ωm) 673K	σ_{dc} (10^{-4}(Ωm)$^{-1}$) 673K	σ_{ac} (10^{-4}(Ωm)$^{-1}$) (50 kHz & 673K)	s_1 673K	s_2 673K	ε′ (100 kHz & 673K)	tanδ (100 kHz & 673K)	β 673K	$\tau_{M''}$ (10^{-4} s) 673K
CT	0.13	6.50	9.79	0.13	-	454	0.376	0.68	3.6 x 10^{-2}
CTNN1	3.93	0.25	0.69	0.21	2.66	747	0.019	0.68	2.2
CTNN2	5.25	0.19	0.65	0.24	2.64	815	0.017	0.69	3.3
CTNN3	10.13	0.11	0.40	0.35	2.47	796	0.012	0.74	6.3
CTNN4	9.74	0.11	0.90	0.73	2.61	808	0.032	0.76	6.3

CTNN samples, respectively, at different temperatures is shown in Figs. 7(a-e) and 8(a-e). There have been reports on the CT sample's dielectric characteristics elsewhere[12]. Both ε' and tan δ show greater dispersion at lower frequencies, on the other hand, for all samples, it approaches a constant level at higher frequencies. The combined effect of charge carrier conduction and dipole orientational relaxation is what causes this behaviour of ε'. Significant values of ε' can be attributed to charged defects, grain boundary effect, interfacial dislocations, oxygen vacancies, and other factors at lower frequencies. Nevertheless, the total polarizability diminishes as the frequency rises because the charge carriers' ability to

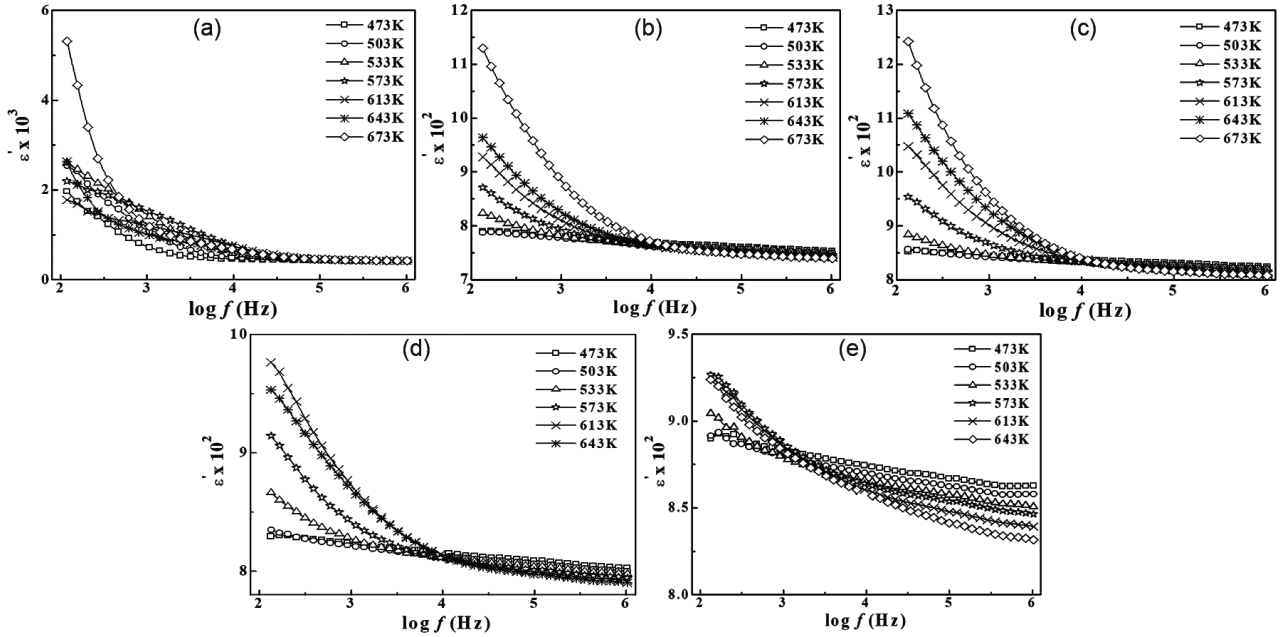

Fig. 7 — Frequency dependence of dielectric permittivity (ε′) for (a) CT (b) CTNN1 (c) CTNN2 (d) CTNN3 (e) CTNN4 samples at different temperatures.

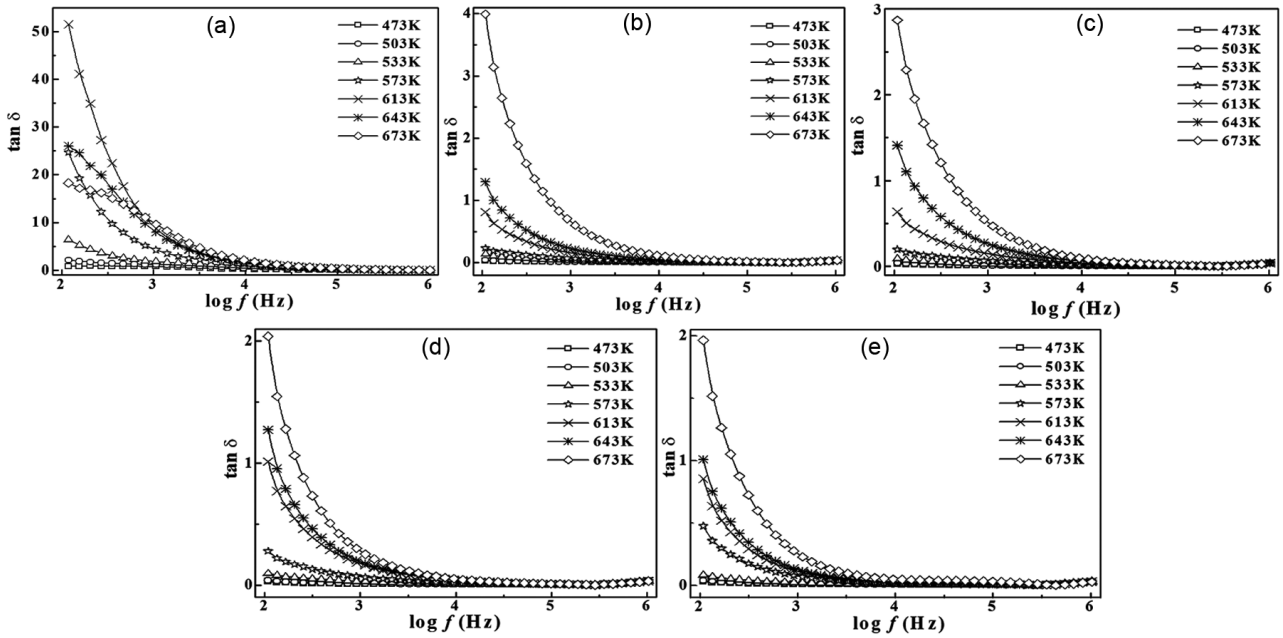

Fig. 8 — Frequency dependence of dielectric losses (tan δ) for (a) CT (b) CTNN1 (c) CTNN2 (d) CTNN3 (e) CTNN4 samples at different temperatures.

trace the applied external field is diminished. This is adequately explained by the combination of Koop's theory of space charge relaxation at the interfaces in heterogeneous systems and Maxwell Wagner type relaxation[32-34]. The observation that both ε' and tan δ values increase with temperature increase is clearly evident from these figures. The polarisation contribution is weak at low temperatures because the electric dipoles are unable to align themselves with the applied field's direction and as a result, the value of ε' is low. With increase in temperature most electric dipoles are able to obtain sufficient thermal energy, which aids in their ability to respond to changes in the external field. As a result, the value of ε' increases because the dipoles' contribution to the polarisation mechanism increases. Since thermally activated charge carriers conduct more readily as temperature rises, there is an increase in losses. Fig. 9 depicts frequency dependence of ε' and tan δ for CT and CTNN samples at 673K. Substitution of $NaNbO_3$ leads to a significant increase in ε′ and decrease in tan δ in the CTNN samples as compared to the CT sample at frequency 100 kHz and temperature 673K (Table 3). With increase of $NaNbO_3$ content in the CT

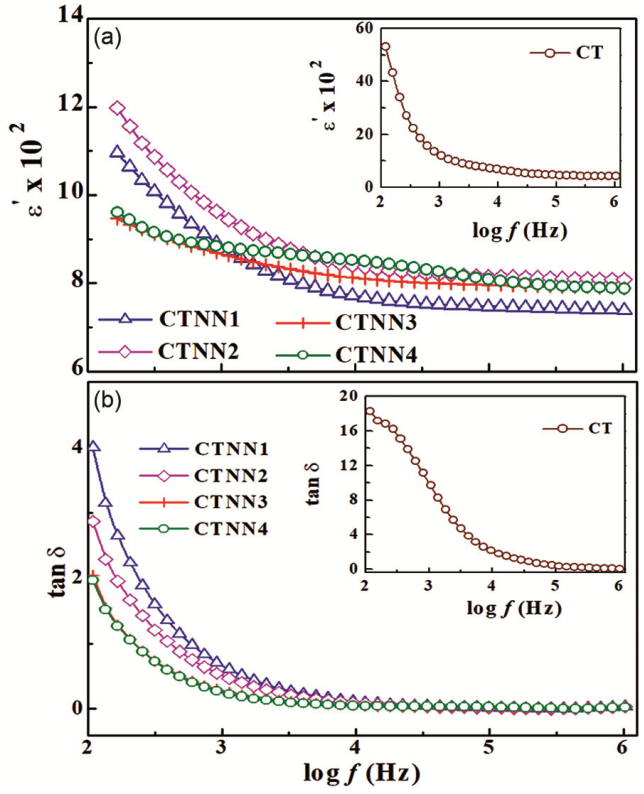

Fig. 9 — Frequency dependence of ε′ and tan δ for CT and CTNN samples at 673K.

matrix dispersive behaviour of ε' decreased rendering stability to ε' as the frequency increases. In titanates, the high sintering temperatures lead to loss of oxygen thus creating oxygen vacancies in the lattice.

$$O_o \leftrightarrow V_o + \tfrac{1}{2} O_2 \quad \ldots(1)$$

$$V_o \leftrightarrow V'_o + e' \quad \ldots(2)$$

$$V'_o \leftrightarrow V''_o + e' \quad \ldots(3)$$

The electrons thus created couple with Ti ($Ti^{4+} \leftrightarrow Ti^{3+} + e^-$) ions giving rise to hopping conduction mechanism. Subsequently when CT matrix is substituted by $NaNbO_3$ charge compensation takes place thus reducing oxygen vacancies in the substituted samples. Oxygen vacancies and other defects participate in conduction mechanism at lower frequencies,therefore at low frequencies a decrease in values of ε′ and tan δ in the $NaNbO_3$ substituted samples is observed. The reduced values of the dielectric parameters at low frequencies *i.e.*, lowering of dispersion indicates lowering of conductivity and hence increased resistivity in the substituted samples.

3.4 Conductivity studies

The temperature-dependent frequency dependence of ac conductivity has been investigated for CT and CTNN samples. The conductivity spectra of the CT and CTNN samples at various temperatures are shown in Fig. 10(a-e). The obtained conductivity spectra can be divided into three portions, as shown in Fig. 10(b). At higher frequencies in the CTNN samples (Fig. 10(b-e) the conductivity values disappear as conductivity demonstrated minus values, due to resonance of permittivity in this region. Only two regions are seen in the conductivity spectra of CT because the third region might be outside the frequency window being investigated. High temperatures and low frequencies are associated with Region I in the figure. The activation of charge carrier hopping towards nearby unoccupied lattice sites, which leads to long-range charge carrier translational motion, is the source of dc conductivity. Region II refers to the frequency values (above critical frequency f_C) where conductivity becomes dispersive in nature. This region's mismatch between the hopping and site relaxation processes results in a

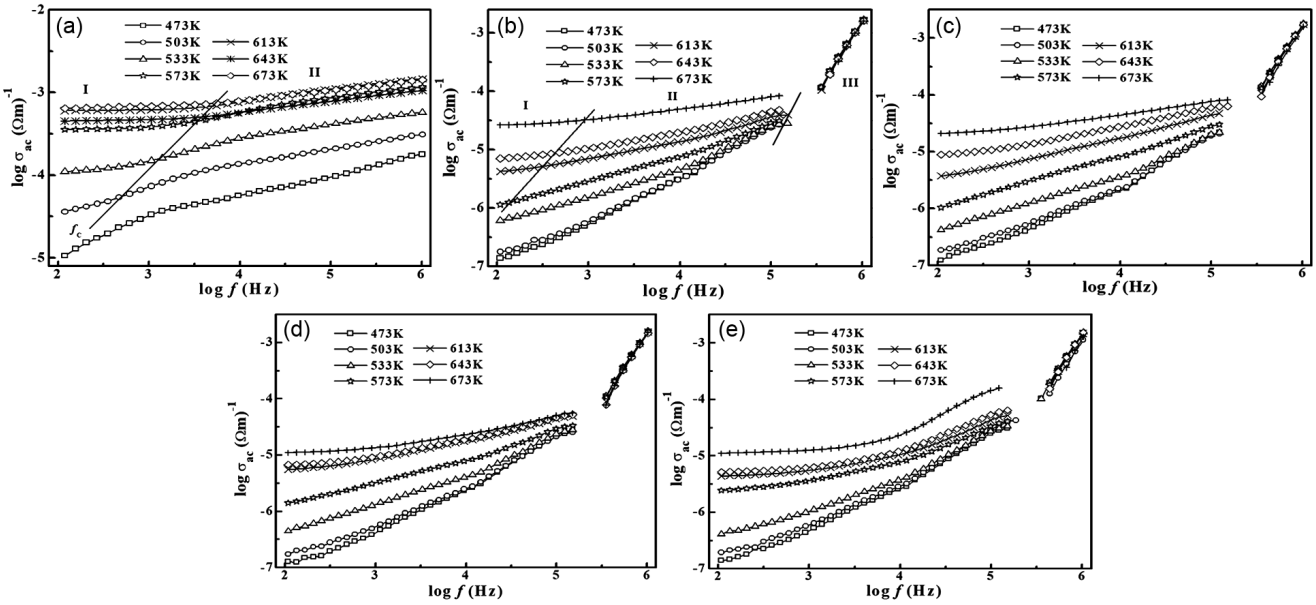

Fig. 10 — Conductivity spectra for (a) CT (b) CTNN1 (c) CTNN2 (d) CTNN3 (e) CTNN4 samples at different temperatures.

predominance of the related back hop rate process, which raises the dispersive conductivity[35]. The critical frequency shifts towards higher frequencies with rise in temperature. The slope (s_1) in this region lies from 0 to 1, is temperature dependent and observed to increase as temperature increases. This may be attributed to the thermal energy attained by the charge carriers as the temperature is increased. Also, it has been noted that with increase of $NaNbO_3$ content in the CT matrix the conductivity spectra become more dispersive at higher frequencies in Region II. Similar pattern is seen in the slope values (s_1) (Table 3). In Region III the temperature sensitivity of the conductivity spectra ceases to exist and all the CTNN samples show temperature independent conductivity spectra. It is clearly observed that the slope values (s_2) in this region are temperature independent. The slope values lie above 2 and show a random behaviour with compositional variation of $NaNbO_3$. The values are listed in Table 3. Fig. 11 illustrates the compositional dependence of dc conductivity (σ_{dc}) at various temperatures. The σ_{dc} values can be computed using the resistance from the intercept on the real axis of the impedance spectra and the sample dimensions. The highest σ_{dc} value is shown by CT sample for all the temperatures. The σ_{dc} values for CTNN samples are almost similar. σ_{dc} values at 673K for all the samples have been listed in Table 3. Introduction of $NaNbO_3$ in the CT matrix leads to a significant change in the σ_{dc} values however concentration of $NaNbO_3$ in CT

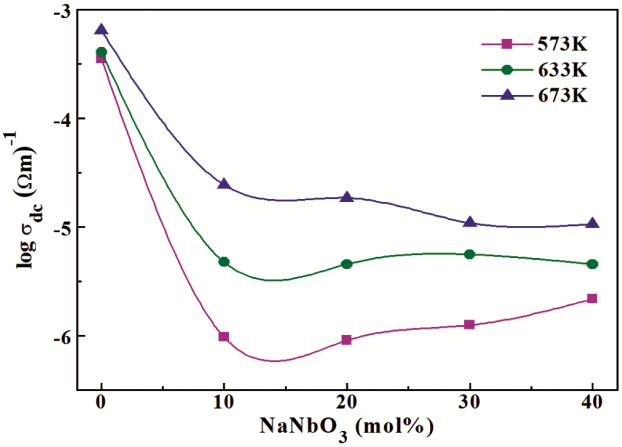

Fig. 11 — Compositional dependence of dc conductivity for CT and CTNN samples.

matrix has an insignificant variation in the conductivity values. This may be related to the charge compensation occurring in the CT lattice by introduction of $NaNbO_3$. Similar behavior was observed for dielectric constant values at low frequencies discussed in the previous section 3.3. The σ_{dc} values for every sample increased with increase in temperature. This may be attributed to the thermal energy gained by the charge carriers when temperature is raised making them more mobile.

3.5 Modulus studies

The electric modulus analysis was performed to get an insight of the electrical transport mechanism taking place in all the prepared samples. The modulus

spectra at 673K for the CT and CTNN samples are shown in Fig. 12. It is observed that as the concentration of $NaNbO_3$ in the CT matrix increased, the electric modulus' peak frequency moved towards lower frequencies. The M″ peak indicates the transition of ions from long range to short range mobility of charge carriers. The region where charge carriers display long-distance mobility is indicated by the frequency region below the M″peak. The charge carriers exhibit localized conduction behaviour and are spatially limited in the potential wells in the frequency band above the M″ peak. The transition of peak frequencies to the left side of the frequency window suggests that the long-range mobility region is lowered and the short-range mobility of ions governs the relaxation process for a large frequency region in the CTNN3 and CTNN4 sample. This may also attribute to decreased conductivity in the CTNN samples. It is also observed in the plots that the samples depict differed peak intensities of M″ curve. The capacitance of the material medium has been found to have an inverse relationship with peak intensity[36]. This implies a change in the capacitance values of each sample with CT showing the lowest capacitance values and CTNN2 the highest. Fig. 13 shows the normalised M″ versus the scaled frequency curves for the CT and CTNN samples at 673K. The plots show that the scaled M″ curves merge for CT, CTNN1 and CTNN2 samples while the CTNN3 and CTNN4 merge with each other only. The same can be confirmed from the stretching parameter (β) values (Table 3). The β values are almost same for CT, CTNN1 and CTNN2 samples while increase for the CTNN3 and CTNN4. The correlation between the hopping ions and the neighbouring ions in a material medium can be interpreted in terms of β[37]. If it approaches unity then it signifies an uncorrelated ionic motion (Debye relaxation) while any deviation from one suggests correlated ionic motion. The values of β for all the samples depict non Debye relaxation process in all the samples. Similar results were obtained for the impedance spectra of the all samples. The increased value of β for CTNN3 and CTNN4 sample indicate a decrease in correlation in the lattice and charge carriers. So the channels of ionic transport in these samples are less active causing higher resistivity values (Table 3). The relaxation times for the samples have been listed in Table 3. The relaxation time were shortest for the CT samples but were of almost similar range for the CTNN samples suggesting faster mobility of ions in CT. Fig. 14 shows the variation of scaled M″ and scaled Z″ curves as function of frequency at 673K. The peak frequencies of M″ and Z″ curves for CT, CTNN1, CTNN2 show mismatching suggesting localised conduction mechanism but for CTNN3 and CTNN4 samples the peaks show almost merged peak frequencies indicating dominance of delocalised conduction mechanism at 673K[38].

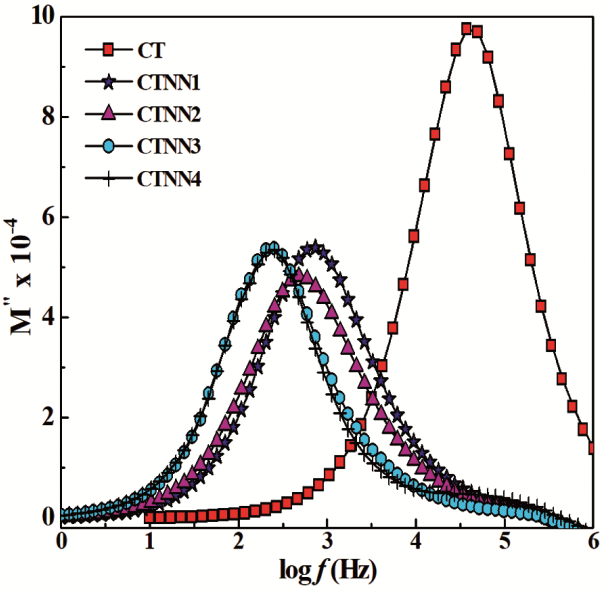

Fig. 12 — Frequency dependence of imaginary modulus (M″) for CT and CTNN samples.

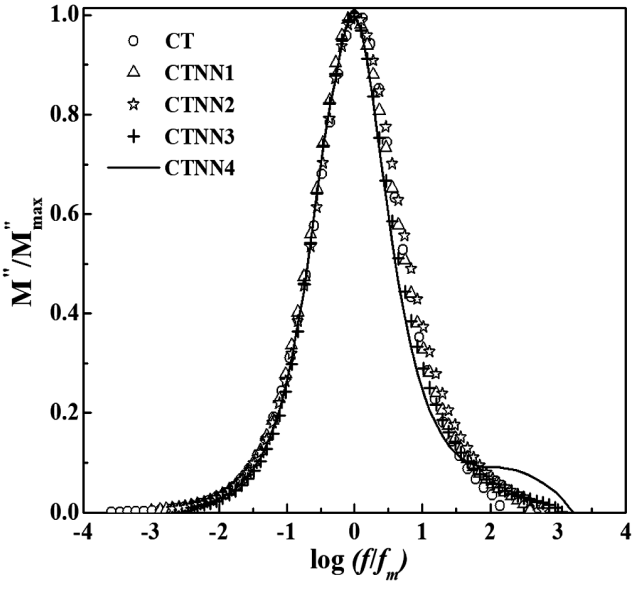

Fig. 13 — Normalised plot of M″/ M''_{max} versus log (f/f_m) for CT and CTNN samples.

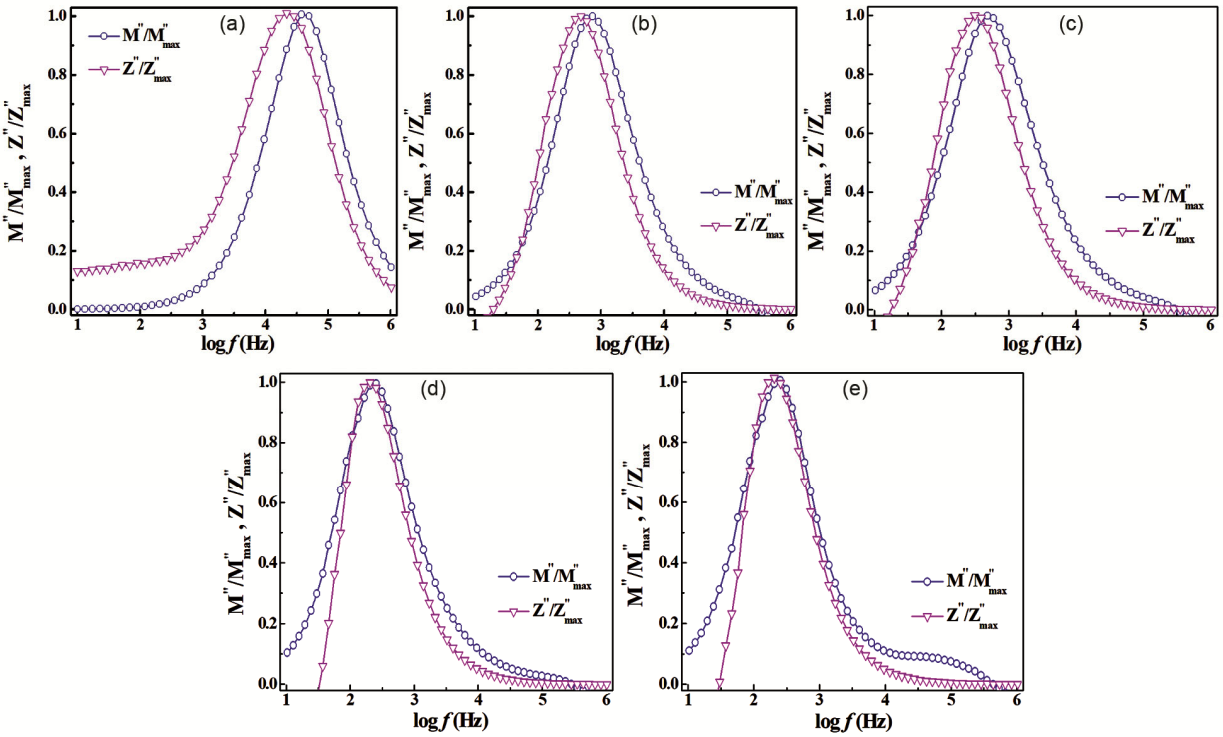

Fig. 14 — Normalised imaginary part of electric modulus and impedance as function of frequency for (a) CT (b) CTNN1 (c) CTNN2 (d) CTNN3 (e) CTNN4 samples at 673K.

4 Conclusion

The impact of $NaNbO_3$ substitution on the electrical and structural characteristics of $CaTiO_3$ ceramics has been documented in the current work. Lead free (1-x)$CaTiO_3$– x$NaNbO_3$ (x = 0, 0.10, 0.20, 0.30, 0.40; CT, CTNN1, CTNN2, CTNN3, CTNN4 respectively) ceramics were prepared by conventional solid state reaction method. Room temperature structural characterization was performed using XRD. Pure crystalline structure for all the samples was confirmed by the same. The Rietveld refinements showed that an orthorhombic structure with Pbnm space group symmetry was present in all the samples. The lattice parameters increased with increase of $NaNbO_3$ substitution indicating an increase in the lattice size. An increase in values of ε′ was observed along with a significant reduction in losses in the CTNN samples. This is a key requirement in electronic devices. The samples exhibited correlation between the charge carriers and lattice. The resistivity significantly increased for the $NaNbO_3$ substituted samples, with the maximum values shown by CTNN3 and CTNN4. The correlation between lattice and charge carriers reduced in the CTNN3 and CTNN4 samples revealed by increased values of stretching coefficient (β).

Acknowledgments

For providing XRD facilities, the authors would like to thank to DST, New Delhi (FIST Scheme). The author (M.S.) expresses gratitude to the Haryana State Counseling Society in Panchkula, Haryana, India, for granting the Sir CV Raman Scholarship.

References

1 Yang L, Kong X, Li F, Hao H , Cheng Z, Liu H, Li J F & Zhang S, *Prog Mater Sci,* 102 (2019) 72.
2 Veerapandiyan V, Benes F, Gindel T & Deluca M, *Materials,* 13 (2020) 5742.
3 Zhang H, Wei T, Zhang Q, Ma W, Fan P, Salamon D, Zhang S T, et al., *J Mater Chem C,* 8 (2020) 16648.
4 Lemanov V V, Sotnikov A V, Smirnova E P, Weihnacht M & Kunze R, *Solid State Commun*, 110 (1999) 611.
5 Hao J, Si W, Xi X X, Guo R, Bhalla A S & Cross L E, *Appl Phys Lett,* 76 (2000) 3100.
6 Cockayne E & Burton B P, *Phy Rev B,* 62 (2000) 3735.
7 Kennedy B J, Howard C J & Chakoumakos B C, *J Phys Condens Matter,* 11 (1999) 1479.
8 Kennedy B J, Howard C J & Chakoumakos B C, *Phys Rev B,* 59 (1999) 4023.
9 Reznitchenko L A, Turik A V, Kuznetsova E M & Sakhnenko V P, *J Phys Condens Matter* 13 (2001) 3875.
10 Megaw H D, *Ferroelectrics,* 7 (1974) 87.
11 Zhang G Z, Zhu D Y, Zhang X S, Zhang L, Yi J Q, Xie B, Zeng Y K, Li Q, Wang Q & Jiang S L , *J Am Ceram Soc,* 98 (2015) 1175.

12 Zhao L, Liu Q, Gao J, Zhang S J & Li J F, *Adv Mater,* 29 (2017) 1701824.
13 Wang H S, Liu Y C, Yang T Q & Zhang S J, *Adv Funct Mater,* 29 (2019) 1807321.
14 Mohapatra P, Fan Z M, Cui J & Tan X L, *J Eur Ceram Soc,* 39 (2019) 4735.
15 Qi H, Zuo R Z, Xie A W, Tian A, Fu J, Zhang Y & Zhang S J, *Adv Funct Mater,* 29 (2019) 1903877.
16 Li S, Hu T F, Nie H C, Fu Z Q, Xu C H, Xu F F, Wang G S & Dong X L, *Energy Storage Mater,* 34 (2021) 417.
17 Li J L, Li F, Xu Z & Zhang S J, *Adv Mater,* 30 (2018) 1802155.
18 Tian A, Zuo R Z, Qi H & Shi M, *J Mater Chem A,* 8 (2020) 8352.
19 Jiang J, Meng X J, Li L, Zhang J, Guo S, Wang J, Hao X H, Zhu H G & Zhang S T, *Chem Eng J,* 422 (2021) 130130.
20 Ye J M, Wang G S, Chen X F & Dong X L, *J Materiomics,* 7 (2021) 339.
21 Tripathi S, Pandey D, Mishra S K & Krishna P S R, *Phys Rev B,* 77 (2008) 052104.
22 Tripathi S, Kumar A, Waghmare U V & Pandey D, *Phys Rev B,* 81 (2010) 212101
23 Larson A C & Dreele R B V, *Lanl Report Laur*, 86 (2000) 748.
24 Toby B H, *J Appl Cryst,* 34 (2001) 210.
25 Sindhu M, Ahlawat N, Sanghi S, Agarwal A, Dahiya R & Ahlawat N N, *Curr App Phys,* 12 (2012) 1429.
26 Toby B H, *Powder Diffr,* 21 (2006) 67.
27 de Souza D A, da Silva P H d A, da Silva F P, Romaguera-Barcelay Y, Ferreira R D, Araujo Junior E A, Nascimento J F d L, da Costa F F, Takeno L L, Leyet R Y, et al., *Colorants*, 3 (2024) 229.
28 Holzwarth U & Gibson N, *Nat Nanotechnol,* 6 (2011) 534.
29 Takeno M L, Nobre F X, Costa F F, Nascimento M V B, *et al*., *ACS Omega*, 9 (2024) 23069.
30 Da Silva P H A, de Souza D A, Filho R L F, Teixeira A P C, Lago R M, Brito W R, Junior E A A, Takeno L L, Morais F S, Nascimento J F d L, Leyet Ruiz Y , Saraiva L B & Nobre F X, *ACS Phys Chem,* XXX (2024) XXX.
31 Bentes S C, Nobre F X, Ferreira R D, Saraiva L B, Mendes O C, Dominguez L A & Ruiz Y L, *Mater Chem Phys,* 314 (2024) 128827.
32 Maxwell J C, *Electricity and Magnetism* (Oxford University Press, Oxford), 1st Edn, 1929.
33 Wagner K W, *Ann Phys,* 40 (1913) 817.
34 Koops C G, *Phys Rev,* 83 (1951) 121.
35 Ortega N, Kumar A, Bhattacharya P, Majumder S B & Katiyar R S, *Phys Rev B,* 77 (2008) 014111.
36 Morrison F D, Sinclair D C & West A R, *J Am Ceram Soc,* 84 (2001) 531.
37 Barsoukov E & Macdonald J R, *Impedance Spectroscopy Theory, Experiment and Applications* (Wiley, New Jersey) 2nd Edn, 2005.
38 Bai W, Chen G, Zhu J Y, Yang J, Lin T, Meng X J, Tang X D, Duan C G & Chu J H, *Appl Phys Lett,* 100 (2012) 082902.